

Received February 12, 2021, accepted March 21, 2021, date of publication April 5, 2021, date of current version April 13, 2021.

Digital Object Identifier 10.1109/ACCESS.2021.3071055

Balance Stability Augmentation for Wheel-Legged Biped Robot Through Arm Acceleration Control

FAHAD RAZA^{ID}, (Graduate Student Member, IEEE), WEI ZHU, (Student Member, IEEE), AND MITSUHIRO HAYASHIBE^{ID}, (Senior Member, IEEE)

Department of Robotics, Graduate School of Engineering, Tohoku University, Sendai 980-8579, Japan

Corresponding author: Fahad Raza (fahadraza@dc.tohoku.ac.jp)

This work was supported by the Japan Society for the Promotion of Science (JSPS) Grant-in-Aid for Scientific Research (B) under Grant 18H01399.

ABSTRACT A self-balancing wheel-legged robot provides higher maneuverability and mobility than legged biped robots. For this reason, wheel-legged systems have attracted enormous interest from academia and commercial sectors in recent years. Most of the past works in this field mainly focused on lower body stabilization. Motivated by the human ability to maintain balance in laborious activities by articulating the arm actively, we explore and analyze the active arm control on top of the wheel-legged system to assist in its balance recovery during external pushes and disturbances. This paper presents a control framework to improve the stability and robustness of an underactuated self-balancing wheel-legged robot using its upper limb arm. Furthermore, we use the centroidal moment pivot (CMP) as a key metric to quantitatively evaluate the effect of the active arm usage on the balance stability improvement of the robot in the ROS-Gazebo environment. The difference from the case of nonusage of arm is verified to clarify the impact of the active arm quantitatively. This concept would lead to the wheel-legged biped robot with an active arm for dual purposes, one is for carrying objects, another is for increasing the balance stability. This point is important for future application in a real-world environment with human-robot interactions.

INDEX TERMS Wheel-legged robots, wheeled inverted pendulum (WIP), underactuated robots, motion control, balance recovery, stability analysis, disturbance rejection.

I. INTRODUCTION

The self-balancing wheel-legged robot provides higher maneuverability, faster speed, and a smaller footprint than legged biped robots. These unique characteristics make them more appealing for indoor environments such as hotel lobbies, banks, hospitals, restaurants, and warehouses. However, there are ongoing research challenges in system modeling, stability analysis, path planning, and motion control because of its self-balancing nature and the non-holonomic constraints of the differential drive. For the same reasons, wheel-legged systems have attracted enormous interest from academia and commercial sectors in recent years.

A. RELATED WORK

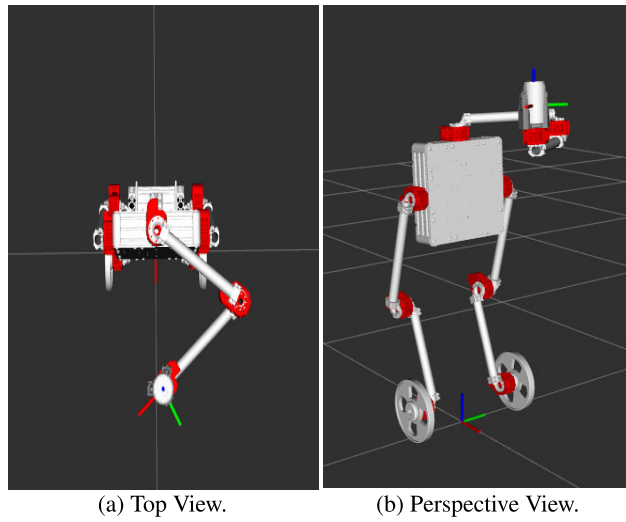
Wheeled inverted pendulum (WIP) robots can be categorized into two major classes: with legs and without legs. A segway is an excellent commercial product of the latter type, which

The associate editor coordinating the review of this manuscript and approving it for publication was Hui Xie^{ID}.

is commonly used to transport humans in the bustling city centers of the modern world. However, WIP robots with legs, also referred to here as wheel-legged robots, are relatively new. In 2017, Boston Dynamics, a robotics company in Massachusetts, USA, introduced its first wheel-legged robot called Handle for warehouse pick and place operations [1].

Early examples of pitch balance and trajectory control of a WIP robot were introduced by Koyanagi *et al.* [2] and Ha and Yuta [3]. Tani *et al.* used WIP robots in the cooperative transportation of objects while satisfying three main requirements: attitude stability of the robot against external disturbances, applying an appropriate force on the transported object, and following the given path [4].

Rufer *et al.* developed a prototype of a two-wheeled vehicle at EPFL, Lausanne and named it JOE [5]. A state-space model-based controller was implemented to balance the robot and control its orientation. The control interface of the vehicle consisted of power-on and emergency switches. The control system was able to safely turn off the vehicle if the pitch angle was more than 100 deg/s.

**FIGURE 1.** Wheel-legged robot with manipulator arm.

Parent *et al.* proposed an intelligent two-wheeled vehicle that could provide on-demand urban taxi services [6]. In another study, Agrawal *et al.* investigated the partial feedback linearization and controllability properties of a WIP robot [7], [8]. A team from Japan developed the first human assistant WIP robot called I-PENTAR and applied a linear quadratic regulator (LQR) for its steering and pitch control [9], [10]. Gloss *et al.* added a humanoid torso on top of a WIP for mobile manipulation [11].

The application of nonlinear sliding-mode controllers to WIP robots has also been extensively studied and reported by the research community. For example, Sekiyama *et al.* implemented two sliding-mode controllers with a novel sliding surface to stabilize a WIP and remove steady-state tracking errors resulting from parameter uncertainties [12]. Lee *et al.* applied a novel integral sliding-mode controller on a two-wheeled inverted pendulum robot that successfully rejected the matched uncertainties and balanced itself on an inclined plane [13]. In another study, Liu *et al.* identified the friction parameters of the drive mechanism in a WIP robot and implemented sliding-mode control to manage the balancing and yaw motions [14].

Recently, whole-body control of WIP robots has also become a subject of interest for the research community. Christensen *et al.* introduced the whole-body control of a WIP humanoid with a manipulator [15]. They performed operational space control of the manipulator by isolating its dynamics from the wheelbase. Theodorou *et al.* further worked on the hierarchical optimization for whole-body control of the WIP robot and successfully implemented it in simulations [16]. Yueyang *et al.* proposed the whole-body control of a WIP robot based on a distributed dynamic model that consisted of the torso model, wheel-leg model, and contact force constraint between the wheels and ground in simulation [17]. However, this robot did not include upper limb arm usage.

TABLE 1. Robot parameters.

Parameters	Description	Value	Unit
m_c	Mass of the robot body	7.5	Kg
m_w	Mass of the robot wheel	0.35	Kg
l	Height of the CoM from the origin of Σ_R	0.5914	m
I_{xx}	Moment of inertia of the robot body in X	0.0878	Kg.m ²
I_{yy}	Moment of inertia of the robot body in Y	0.0347	Kg.m ²
I_{zz}	Moment of inertia of the robot body in Z	0.0632	Kg.m ²
I_{wa}	Moment of inertia of the robot wheel about the wheel axis	0.0018	Kg.m ²
I_{wd}	Moment of inertia of the robot wheel about its diameter	0.000929	Kg.m ²
I_{ma}	Moment of inertia of the motor rotor about its axis	$1.04E - 7$	Kg.m ²
I_{md}	Moment of inertia of the motor rotor about its diameter	0.0	Kg.m ²
g	Gravitational acceleration constant	9.81	m/s ²
r_w	Wheel radius	0.1016	m
b	Distance between the origin of Σ_R and the center of the wheel	0.2150	m
γ	Gear reduction ratio	1	
c_r, c_l	Viscosity coefficients of left and right wheels	0.25	Nm/(rad/sec)
I_1	Moment of inertia of the arm link-1	0.018	Kg.m ²
I_2	Moment of inertia of the arm link-2	0.0339	Kg.m ²
l_1	Length of the arm link-1	0.3	m
l_2	Length of the arm link-2	0.3	m
l_{g1}	Distance of CoM of the arm link-1 from its origin	0.3	m
l_{g2}	Distance of CoM of the arm link-2 from its origin	0.3	m
m_1	Mass of the arm link-1	0.6	Kg
m_2	Mass of the arm link-2	1.13	Kg

In another engaging simulation study, Tsagarakis *et al.* explored the question of whether a humanoid robot can ride a Segway type WIP robot [18]. They applied quadratic optimization to generate humanoid whole-body joint torques to successfully produce balancing on a WIP platform. More recently, Siegwart *et al.* from ETH, Zurich developed a WIP jumping robot that used an LQR controller for its pitch balance. Moreover, a rolling constraint was also added to the robot to increase its robustness against curves and lateral disturbances [19], [20]. Caporale *et al.* demonstrated strong inertial coupling between the wheelbase and pitch dynamics of a humanoid WIP robot and utilized a nonlinear computed-torque controller in quasi-velocities for stabilization [21].

Kwon *et al.* presented a nonlinear optimal control design based on the state-dependent Riccati equation (SDRE) [22]. The proposed control framework was a nonlinear form of the LQR and demonstrated better performance than a conventional LQR in controlling the forward position, pitch, and yaw of a two-wheeled inverted pendulum mobile robot. In a more

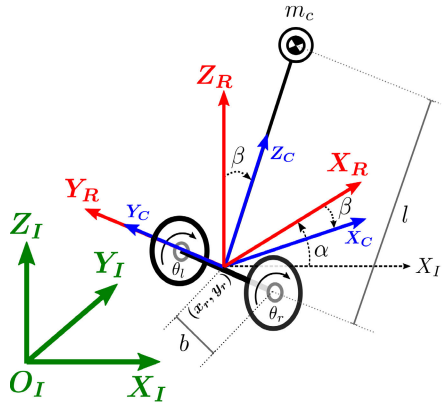


FIGURE 2. Lower-body dynamic model.

recent study, Ming *et al.* proposed a new SDRE controller design scheme for WIP robots [23]. The study analyzed the SDRE method from a computational perspective, improving the online computational performance by avoiding too many solvability inspections of the algebraic Riccati equations.

B. MOTIVATION

Balancing of WIP robots is of foremost importance for the safety of the agents around the robot and smooth human-robot interaction. It is clear from the above discussion that most of the past work in this field focused only on the lower body stabilization of WIP systems. However, recent studies suggest that humans extensively use upper-body movements to dynamically balance during challenging tasks [24]. In this study, we propose a novel balance recovery method for a wheel-legged robot with active usage of an arm manipulator on top of the lower limb. Furthermore, we evaluate the real effect of the upper limb motion of the robot on its stability during external disturbances. For this reason, the centroidal moment pivot (CMP), a key criterion for measuring the stability of humans (also known as the zero rate of angular momentum) is applied to this study [25], [26].

II. DYNAMIC MODELING AND MOTION CONTROL

This section briefly details the dynamic modeling and control of the robot and its manipulator arm. The parameters of the robot are listed in Table 1. For more detailed work on the dynamic model of the robot, the reader is encouraged to review our previous studies on the lower-body motion controller [27], [28].

A. LOWER-BODY MODELING AND CONTROL

For simplification purposes, the wheel-legged robot shown in Fig. 1 is modeled as an inverted pendulum without its arm manipulator. Three coordinate frames, Σ_I , Σ_R , and Σ_C are used to derive the equations of motion of the robot, as shown in Fig. 2. Σ_I is the ground fixed inertial frame and Σ_R is fixed to the robot base. Σ_C is fixed to the center of mass (CoM) of the robot and its origin coincides with Σ_R . Moreover, we assumed the following conditions:

- The wheels of the robot do not slip on the ground.
- The wheels are rigid and nondeformable cylindrical disks.
- The robot body is symmetrical about its vertical axis.
- The legs of the robot are massless.

The pitch angle of the robot (β) is the angle between the Z-axes of the robot base frame Σ_R and the CoM frame Σ_C . The yaw rotation of the robot is described by the angle α , which is the angle between the corresponding X-axes of the Σ_R frame and inertial frame Σ_I .

The total kinetic energy of the robot center of mass is:

$$T_c = \frac{1}{2}m_c V_c^T V_c + \frac{1}{2} c \Omega_c^T I_c c \Omega_c, \quad (1)$$

where m_c is the mass of the robot body, V_c and $c \Omega_c$ are the linear and angular velocities of the CoM in the Σ_I and Σ_C frames, respectively, and I_c is the inertia matrix of the robot body taken at its CoM.

The Kinetic energy of the robot wheels is:

$$T_w = \frac{1}{2}m_w r_w^2 \dot{\theta}_r^2 + \frac{1}{2}m_w r_w^2 \dot{\theta}_l^2 + \frac{1}{2}(I_{wa} + I_{ma}\gamma^2)(\dot{\theta}_r^2 + \dot{\theta}_l^2) + (I_{wd} + I_{md})\dot{\alpha}^2, \quad (2)$$

where m_w is the wheel mass, r_w is the wheel radius, θ_r and θ_l denote the angular displacements of the right and left wheels, respectively, γ represents the gear reduction ratio, I_{wa} and I_{wd} are the moments of inertia of the wheel about its axis and diameter, respectively, and I_{ma} and I_{md} are the moments of inertia of the motor rotor about its axis and diameter, respectively.

We assumed that the wheels always remained in contact with the ground, so the potential energy of the wheels remains at zero. The potential energy of the robot's CoM is denoted by:

$$U_c = m_c g l \cos(\beta), \quad (3)$$

where g is the gravitational acceleration constant.

Rayleigh's dissipation function due to a wheel's viscous friction is represented by:

$$F = \frac{1}{2}c_r(\dot{\theta}_r - \dot{\beta})^2 + \frac{1}{2}c_l(\dot{\theta}_l - \dot{\beta})^2, \quad (4)$$

where c_r and c_l are the viscosity coefficients of the right and left wheels, respectively.

We apply a Lagrangian formulation to derive the dynamic equation of the robot. The Lagrangian of a system is obtained from the difference between the kinetic and potential energies, expressed as:

$$\begin{aligned} L &= K.E - P.E \\ &= T_c + T_w - U_c. \end{aligned} \quad (5)$$

The equations of motion of the whole system are then calculated by solving the following:

$$\frac{d}{dt} \left(\frac{\partial L}{\partial \dot{q}_i} \right) - \frac{\partial L}{\partial q_i} + \frac{\partial F}{\partial \dot{q}_i} = Q_i, \quad (6)$$

where q is the vector of the generalized coordinates and Q generalized forces. The generalized coordinate vector is $q = [{}_I x_r \ {}_I y_r \ \alpha \ \beta \ \theta_r \ \theta_l]^T$, where ${}_I x_r$ and ${}_I y_r$ denote the location of the robot's base in the inertial frame Σ_I . Equation (6) presents the well-known manipulator equations of a robot with nonholonomic constraints:

$$M(q)\ddot{q} + V\dot{q} + H(q, \dot{q}) + G = E\tau_w + A(q)^T\lambda, \quad (7)$$

where $M(q) \in \mathbb{R}^{6 \times 6}$ is the inertia matrix, $V \in \mathbb{R}^{6 \times 6}$ is the square matrix of viscous friction terms, $H(q, \dot{q}) \in \mathbb{R}^6$ is the vector of the Coriolis and centrifugal terms, $G \in \mathbb{R}^6$ is the vector of the gravitational forces, $E \in \mathbb{R}^{6 \times 2}$ is the torque selection matrix, $\tau_w \in \mathbb{R}^2$ is the vector of the wheel joint torques, and $A(q)^T\lambda$ represents the vector of the reaction forces at the generalized coordinate level.

To remove the Lagrange multiplier vector λ from (7), as explained in [29], a new vector $u \in \mathbb{R}^3$ of *pseudo-velocities* is defined such that:

$$\dot{q} = S(q)u, \quad (8)$$

where $S(q) \in \mathbb{R}^{6 \times 3}$ is a full rank matrix that lies in the null space of $A(q)$. $u = [v \ \dot{\alpha} \ \dot{\beta}]^T$, where v is the forward velocity of the robot in the X_R direction. We obtain the reduced-order equations of motion in the following form:

$$\hat{M}\dot{u} + \hat{V}u + \hat{H}(u) + \hat{G} = \hat{E}\tau_w, \quad (9)$$

where $\hat{M} = S(q)^T M(q) S(q)$ is positive definite, $\hat{V} = S(q)^T V S(q)$, $\hat{H}(u) = S(q)^T [M(q)S(q)u + H(q, \dot{q})]$, $\hat{G} = S(q)^T G$, and $\hat{E} = S(q)^T E$.

As θ_r and θ_l are decoupled from other state variables, we define a configuration vector $q_r = [p \ \alpha \ \beta]^T$ as an actual control variable for the lower-body control, where $p = {}_I x_r \cos(\alpha) + {}_I y_r \sin(\alpha)$.

LINEAR QUADRATIC REGULATOR

We designed and implemented an LQR controller to control and balance the lower body of the robot. First, we linearize (9) about the equilibrium point ($\beta = 0$) of the robot, making the following small-angle approximations:

$$\begin{aligned} \sin(*) &\simeq (*), \\ \sin^2(*) &\simeq 0, \\ \cos(*) &\simeq 1, \\ (*)^2 &\simeq 0, \\ (*)(*) &\simeq 0. \end{aligned}$$

\hat{H} is eliminated from Eq. (9) because of the linearization, and we then obtain:

$$\hat{M}\dot{u} + \hat{V}u + \hat{G} = \hat{E}\tau, \quad (10)$$

After linearizing the equations of motion, we define the state-space model of the system that converts the N^{th} -order system dynamics into a system of N first-order differential equations.

$$\dot{X} = AX + BU$$

$$Y = CX + DU, \quad (11)$$

where $X = [q_r \ u]^T$ is the state vector, $Y \in \mathbb{R}^6$ is the output vector of the system, and $U \in \mathbb{R}^2$ is the system input, i.e., the wheel torques. The constant matrices A , B , C , and D are the system dynamics, input, output, and feedforward matrices, respectively.

The state-feedback control law is represented by:

$$U = ref. - K_{lqr}X, \quad (12)$$

where $ref.$ is the reference signal.

LQR places the poles so that the closed-loop system optimizes the following cost function:

$$J_{lqr} = \int_0^\infty [X(t)^T Q X(t) + U(t)^T R U(t)] dt,$$

Here, Q and R are used as weighting matrices for the system states and inputs, respectively.

For a continuous time invariant system, the LQR feedback gain is:

$$K_{lqr} = R^{-1}B^T P,$$

where P is obtained by solving the following algebraic Riccati equation:

$$A^T P + PA - PBR^{-1}B^T P + Q = 0 \quad (13)$$

To obtain the LQR feedback gain vector K_{lqr} by solving (13), we use the *MATLAB* (Mathworks Inc., Natick, MA, USA) command:

$$\gg K_{lqr} = lqr(A, B, Q, R)$$

After obtaining the A and B matrices using the robot's parameters from Table 1, as well as selecting the Q and R matrices through trial-and-error to improve the controller's performance, the following feedback gain is obtained: K_{lqr} , as shown at the bottom of the next page.

B. ARM MANIPULATOR MODELING AND CONTROL

The manipulator arm is decoupled from the rest of the robot body and modeled separately from the lower body of the robot. We used the resolved acceleration control method to manipulate the end-effector position and acceleration in the Cartesian plane [30].

A schematic of the manipulator is shown in Fig. 3. For simplification purposes, we assumed that the masses of the links act as point masses and are located at the end of each link. Furthermore, the CoM of each link was located at the far end of the corresponding link. In addition, friction was considered negligible. The rigid-body dynamics equation for a two-link arm can easily be derived using the Lagrangian formulation and is generally presented in the following form:

$$\tau_m = M(\theta)\ddot{\theta} + h(\theta, \dot{\theta}) + g(\theta), \quad (14)$$

where τ_m is the vector of the joint torques τ_1 and τ_2 , θ is the vector of the joint angles θ_1 and θ_2 , $h(\theta, \dot{\theta})$ is the vector of the Coriolis and centrifugal forces, $g(\theta)$ is the vector of

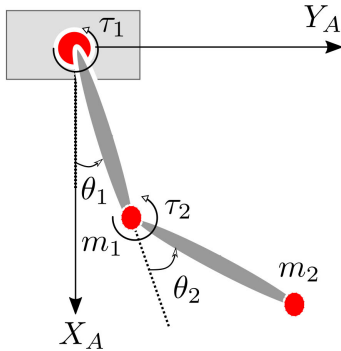


FIGURE 3. Schematic of the arm manipulator on top of the lower limb of the wheel-legged robot.

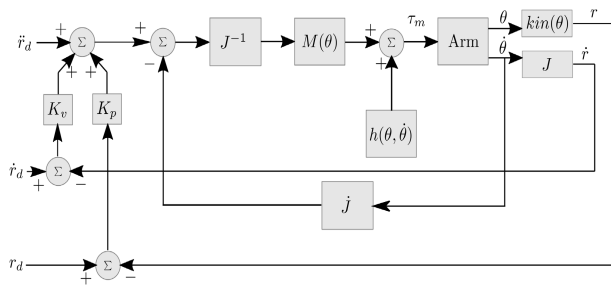


FIGURE 4. Arm manipulator control scheme.

the gravitational forces, and $M(\theta)$ is the inertia matrix that is symmetric, positive definite, and always invertible.

$$M(\theta) = \begin{bmatrix} M_{11} & M_{12} \\ M_{21} & M_{22} \end{bmatrix}$$

where

$$\begin{aligned} M_{11} &= I_1 + I_2 + m_1 l_{g1}^2 \\ &\quad + m_2 (l_1^2 + l_{g2}^2 + 2l_1 l_{g2} + 2l_1 l_{g2} \cos(\theta_2)) \\ M_{12} &= M_{21} = I_2 + m_2 (l_{g2}^2 + l_1 l_{g2} \cos(\theta_2)) \\ M_{22} &= I_2 + m_2 l_{g2}^2 \end{aligned}$$

The manipulator works in the horizontal plane, so we can ignore the gravitational forces and (14) reduces to:

$$\tau_m = M(\theta)\ddot{\theta} + \mathbf{h}(\theta, \dot{\theta}), \quad (15)$$

The vector of the Coriolis and centrifugal forces is:

$$\mathbf{h}(\theta, \dot{\theta}) = \begin{bmatrix} -m_2 l_1 l_{g2} \dot{\theta}_2 (2\dot{\theta}_1 + \dot{\theta}_2) \sin(\theta_2) \\ m_2 l_1 l_{g2} \dot{\theta}_1^2 \sin(\theta_2) \end{bmatrix}$$

RESOLVED ACCELERATION CONTROL

To control the end-effector position, velocity, and acceleration in the Cartesian plane, we must transform (15) from joint-space variables to Cartesian space variables. This is achieved

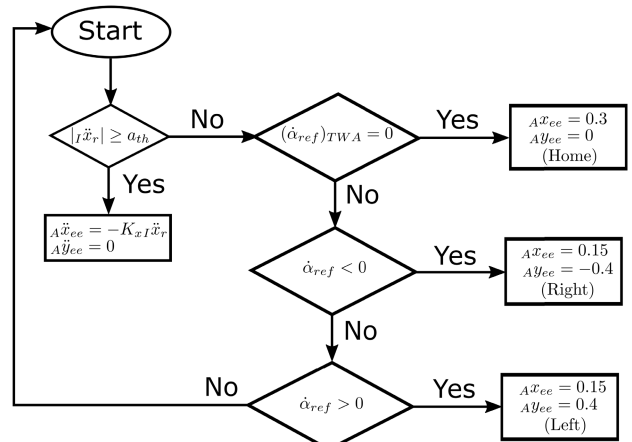


FIGURE 5. State machine flowchart for active arm usage.

by using the Jacobian matrix that relates the joint velocities of the manipulator to the Cartesian velocities of the end-effector, as follows:

$$\dot{\mathbf{r}} = \begin{bmatrix} A\dot{x}_{ee} \\ A\dot{y}_{ee} \end{bmatrix} = J \begin{bmatrix} \dot{\theta}_1 \\ \dot{\theta}_2 \end{bmatrix}$$

where the closed-form Jacobian matrix is denoted as:

$$J = \begin{bmatrix} -l_1 \sin(\theta_1) - l_2 \sin(\theta_1 + \theta_2) & -l_2 \sin(\theta_1 + \theta_2) \\ l_1 \cos(\theta_1) + l_2 \cos(\theta_1 + \theta_2) & l_2 \cos(\theta_1 + \theta_2) \end{bmatrix}$$

Equation (15) then becomes:

$$\tau_m = M(\theta)J^{-1}(\ddot{\mathbf{r}} - j\dot{\theta}) + \mathbf{h}(\theta, \dot{\theta}) \quad (16)$$

Equation (16) can be used to design a simple controller that reduces the error between the desired and actual position, velocity, and acceleration of the end-effector. Here, we choose a simple proportional derivative (PD) control scheme that results in:

$$\begin{aligned} \tau_m &= M(\theta)J^{-1}[\ddot{\mathbf{r}}_d + \mathbf{K}_v(\dot{\mathbf{r}}_d - \dot{\mathbf{r}}) + \mathbf{K}_p(\mathbf{r}_d - \mathbf{r}) - j\dot{\theta}] \\ &\quad + \mathbf{h}(\theta, \dot{\theta}) \end{aligned} \quad (17)$$

where $\ddot{\mathbf{r}}_d$ is the vector of desired accelerations in the Cartesian plane, $\dot{\mathbf{r}}_d$ is the vector of the desired velocities, \mathbf{r}_d is the vector of the desired positions, and \mathbf{K}_p and \mathbf{K}_v are the PD controller gains for the position and velocity, respectively. Suitable PD controller gains were obtained through trial and error in the simulations. Figure 4 presents the overall controller scheme for the manipulator arm of the robot.

III. FINITE-STATE MACHINE

To control the end-effector acceleration and position to cancel out or mitigate the external disturbances on the robot, we design a finite-state machine, as shown in Fig. 5. First,

$$K_{lqr} = \begin{bmatrix} -0.7071 & 0.7071 & -16.2331 & -3.1751 & 0.2016 & -3.5082 \\ -0.7071 & -0.7071 & -16.2331 & -3.1751 & -0.2016 & -3.5082 \end{bmatrix}.$$

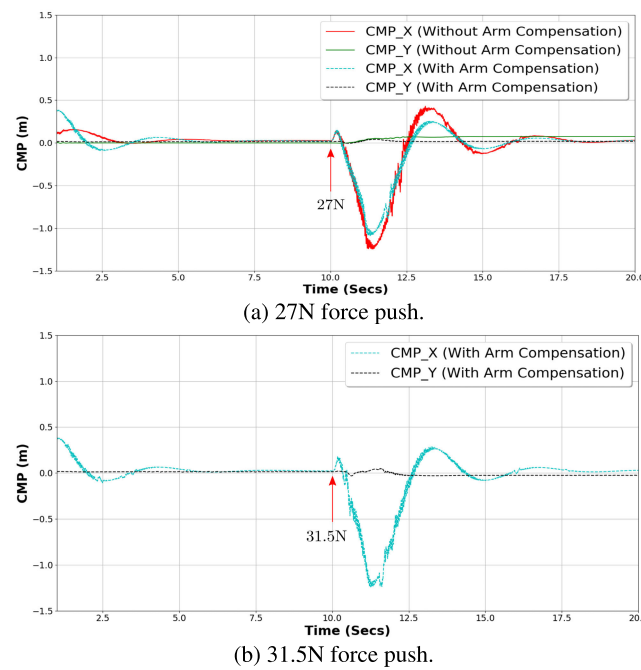


FIGURE 6. Temporal variation of the centroidal moment pivot (CMP) point under the translational disturbances while the robot is holding a typical can.

we check the translational acceleration of the robot, and if it is greater than a certain threshold a_{th} , then the end-effector accelerates in the opposite direction of the robot's translational acceleration with some proportional gain K_x .

Second, when the robot traverses a curve, it rotates the end-effector toward the center of the curvature to deal with outward inertial forces such as centrifugal force. However, to distinguish whether the robot is traversing a curve or it is merely a small rotation, we take the time-weighted average of the reference yaw velocity $(\dot{\alpha}_{ref})_{TWA}$ over the period of a half-second. If $(\dot{\alpha}_{ref})_{TWA}$ is zero, which indicates that the robot is not traversing a curve, then the end-effector remains at its home position.

In this manner, if the robot rotates in the clockwise direction, the end-effector moves toward the right side of the robot, and when the robot rotates in the counterclockwise direction, the end-effector shifts toward the left side.

IV. CENTROIDAL MOMENT PIVOT

Goswami and Herr independently introduced the centroidal moment pivot (CMP) as a useful criterion for the analysis and posture stability measure of biped robots [31], [32]. CMP is derived from the rate of change of the angular momentum \dot{H}_G , which is applicable only when a robot is walking on a planar surface. The loss of balance in biped robots simply means that \dot{H}_G is non-zero. We used this key stability criterion for the first time for a biped wheel-legged robot.

CMP is defined as the robot's CoM projection point on the ground along the resultant ground reaction force [33], [34]. In other words, it is the point where the reaction force needs

to be applied to result in zero \dot{H}_G . Thus, the amount of CMP deviation from the body center can indicate the intensity of the whole-body balance instability, and hence it is used to evaluate the resultant balancing stability in this study. CMP (p_f) is derived from the position of the CoM of the robot, ground reaction force vector, and a normal vector, as follows:

$$p_f = \frac{(\mathbf{p}_0 - \mathbf{c}) \cdot \mathbf{n}}{\mathbf{f} \cdot \mathbf{n}} \mathbf{f} + \mathbf{c} \quad (18)$$

where \mathbf{c} is the position of the CoM, \mathbf{n} is the normal vector to the ground plane, \mathbf{f} is the vector of the ground reaction forces, and \mathbf{p}_0 is the ground level.

There are no sensors available to measure the ground reaction force directly from the robot, so we approximately calculate \mathbf{f} as follows:

$$\mathbf{f} = m(\ddot{\mathbf{c}} - \mathbf{g}) \quad (19)$$

where $\ddot{\mathbf{c}}$ is the acceleration of the CoM, m is the total mass of the robot, and \mathbf{g} is the vector of gravitational acceleration.

For a planar surface, (18) can be reduced to:

$$p_f = \frac{p_0 - c_z}{f_z} f + c \quad (20)$$

where c_z and f_z are the vertical components of the CoM position and ground reaction force, respectively.

V. SIMULATION VALIDATION AND RESULTS

In this section, we present the details of the simulation setup and experimental results. The bipedal wheel-legged robot was designed and simulated using the Gazebo simulator, and the robot operating system (ROS) was used to implement the control framework in C++ [35], [36]. The lower body and manipulator controls of the robot were decoupled from each other, so they were implemented separately. In all experiments, the robot carried a can of cola in its manipulator hand to simulate a real-world example, as shown in Fig. 1b. The stretched arm of the robot was 0.6 m in length, and in all experiments the initial arm posture remained at the home configuration ($Ax_{ee} = 0.3$, $Ay_{ee} = 0$) to hold an object in front of the robot body and to allow ample room for arm motion.

A. TRANSLATIONAL DISTURBANCE

We began by applying translational pushes to the robot in the $-X_C$ direction, and the arm is actively used to cancel these external disturbances as shown in Fig. 7. Multiple experiments were performed to characterize the effects of arm acceleration on the CMP stability of the robot. Additionally, to statistically improve the results, each experiment was performed five times and the mean errors and standard deviations were computed. The results are presented in Table 2 that compares the fixed arm cases and the active arm cases together with percentage differences information. As force was applied to the sagittal plane of the robot, errors were measured as time integration in its translational direction to measure the overall amount of instability over the time. Furthermore, to observe the implications of object mass on

system stability, we divided the experiments into two categories. The first set of tests was performed with endpoint mass of 360g assuming that the robot is holding a typical canned drink. In the second set of experiments, we doubled the endpoint mass to 720g and its respective moment of inertia.

In the first experiment, we used the threshold force of 20 N that could activate the arm acceleration to cancel the external translational disturbances. The linear force was applied to the robot body at time $t = 10\text{s}$ of the experiment, first in the fixed arm posture and then with the end-effector acceleration control. The results demonstrate that the arm acceleration to cancel the effects of the external push reduced the CMP mean error by more than 12% over the fixed arm configuration. This difference is more pronounced in the case of the heavy can, where the CMP error was reduced by over 18%.

In the second experiment, the external force applied was 23 N. When the robot was carrying a typical can the CMP error decreased from 2.2044 m.s to 1.8885 m.s thanks to the active arm usage. Likewise, when the can mass was doubled, the CMP error decreased further from 2.2098 m.s to 1.7901 m.s. In the typical and doubled examples, the errors were reduced by 14.33% and 18.99%, respectively.

Likewise, the same experiments were repeated for 25 and 27 N forces. The results of the 27 N force experiment, in which the robot is holding a typical can, are shown in Fig. 6a for both the fixed arm case and arm acceleration method. It is clear that the robot successfully maintains a small CMP error while using its arm compared to when the arm is fixed. We found that without using the end-effector acceleration(the fixed arm configuration) the robot could only sustain the maximum translational push of 27 N. However, the end-effector acceleration could increase its ability to maintain balance for a push of up to 31.5 N for a typical can and 32.5 N when the can mass was doubled. Fig. 6b demonstrates the CMP of the robot when a force of 31.5 N was applied to the front of its body.

B. LATERAL DISTURBANCE

When a body moves around a fixed point in a circular path, an inertial force acts radially outwards on the body, called the centrifugal force. This force, along with external lateral forces, can cause rollover accidents on roads if vehicles try to navigate sharp curved paths at higher speeds. However, this phenomenon is not limited to road vehicles, as modern mobile robots are equally susceptible to these forces. To counter the effects of centrifugal force on a wheel-legged robot in circular trajectories, Siegwart *et al.* proposed regulating the roll angle of the robot using its knee joints as a function of the zero-moment point [20].

When humans ride a bike over a sharp curvature, they anticipate the potential centrifugal force in order to increase the stability margin. Inspired by this fact, we propose active arm usage for traversing curved trajectories by the wheel-legged robot. In this section, we present the results of the proposed method in which the robot uses its manipulator arm

TABLE 2. Balance stability indicated by the time integrated CMP errors as a result of the forces applied to the robot body, along with the standard deviations. The smaller CMP errors indicate higher balance stability. e_x denotes the CMP error in the robot's sagittal plane. In contrast, N/A implies that the robot falls over as a result of the corresponding external force. For all cases, the active arm usage improves the balance stability as indicated by the percentage change compared to the fixed arm case.

External Force	Endpoint Mass 360g		
	Fixed Arm		Percent Change
	$\int e_x dt$	$\int e_x dt$	
20N	1.9582±0.0062	1.7076±0.0042	12.7948%
23N	2.2044±0.0161	1.8885±0.0019	14.3302%
25N	2.3469±0.0083	2.0213±0.0102	13.8746%
27N	2.4931±0.0226	2.0539±0.0164	17.6137%
31.5N	N/A	2.2887±0.0221	-
External Force	Endpoint Mass 720g		
	Fixed Arm		Percent Change
	$\int e_x dt$	$\int e_x dt$	
20N	1.9778±0.0073	1.6207±0.0008	18.0554%
23N	2.2098±0.0120	1.7901±0.0067	18.9938%
25N	2.3529±0.0078	1.9139±0.0072	18.6565%
27N	2.4983±0.0045	2.0401±0.0123	18.3414%
32.5N	N/A	2.2160±0.0136	-

to move its CoM and to shift the balance point toward the center of the circular path, thereby improving its robustness against lateral forces.

Figure 8 shows the experiment in which the robot traverses an infinity-loop shape trajectory at different speeds. We chose the infinity-loop shaped trajectory because it provides a good combination of linear and circular paths. First, we start with the normal speed in which the maximum translational velocity is 0.3 m/s and maximum yaw velocity is 0.3 rads/s. Figures 8a and 8b show the experiments in a ROS-Gazebo environment for the fixed arm and active arm cases, respectively. We can clearly see that the robot follows the target trajectory completely in both cases when it is moving rather slowly. However, it is evident from Fig. 8b that by moving the arm towards the center of the curvature, the CMP not only remains inside the loop but also has a bigger margin from the target trajectory than in the fixed arm case (Fig. 8a).

In the second experiment, we enhanced the maximum translational velocity of the robot to 0.7 m/s and the maximum yaw velocity to 0.6 rads/s. The inertial forces on the robot increased as the robot speed increased on the curves. Additionally, the CMP moved radially outwards, as seen in Figs. 8c and 8d. Furthermore, in both cases it is clear that the robot does not closely follow the target trajectory and its path diverges from the goal trajectory because of the increased speed and consequential inertial forces. Nevertheless, Fig. 8d suggests that the robot has a higher stability margin for the lateral disturbances as the CMP remains inside the target trajectory and closer toward the center of the curvature.

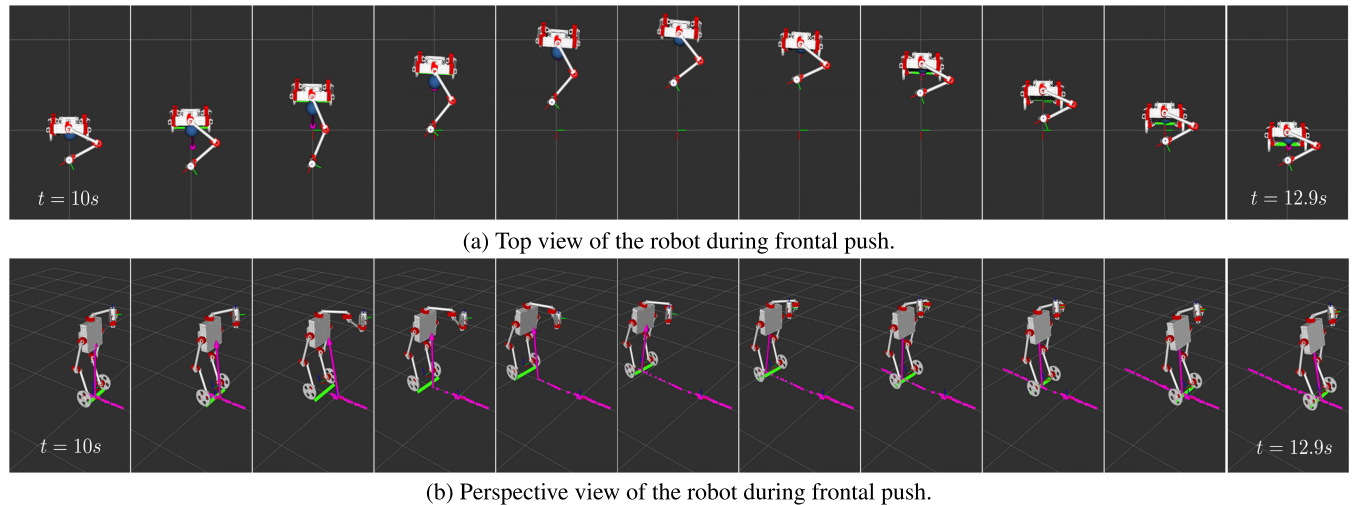


FIGURE 7. Wheel-legged robot reacting to the frontal push of 27N with active arm acceleration control. In the first scene, the disturbance is applied to the robot's front side. The arm starts to make extension action as it is reacting actively to cancel this disturbance. The blue sphere shows the total robot CoM and the pink sphere shows the CMP point. Just after the push, the mismatch between the CMP and the ground projected CoM is large due to the external disturbance. However, after making the arm extension action, this mismatch is disappeared in a few scenes, which demonstrates the balance recovery.

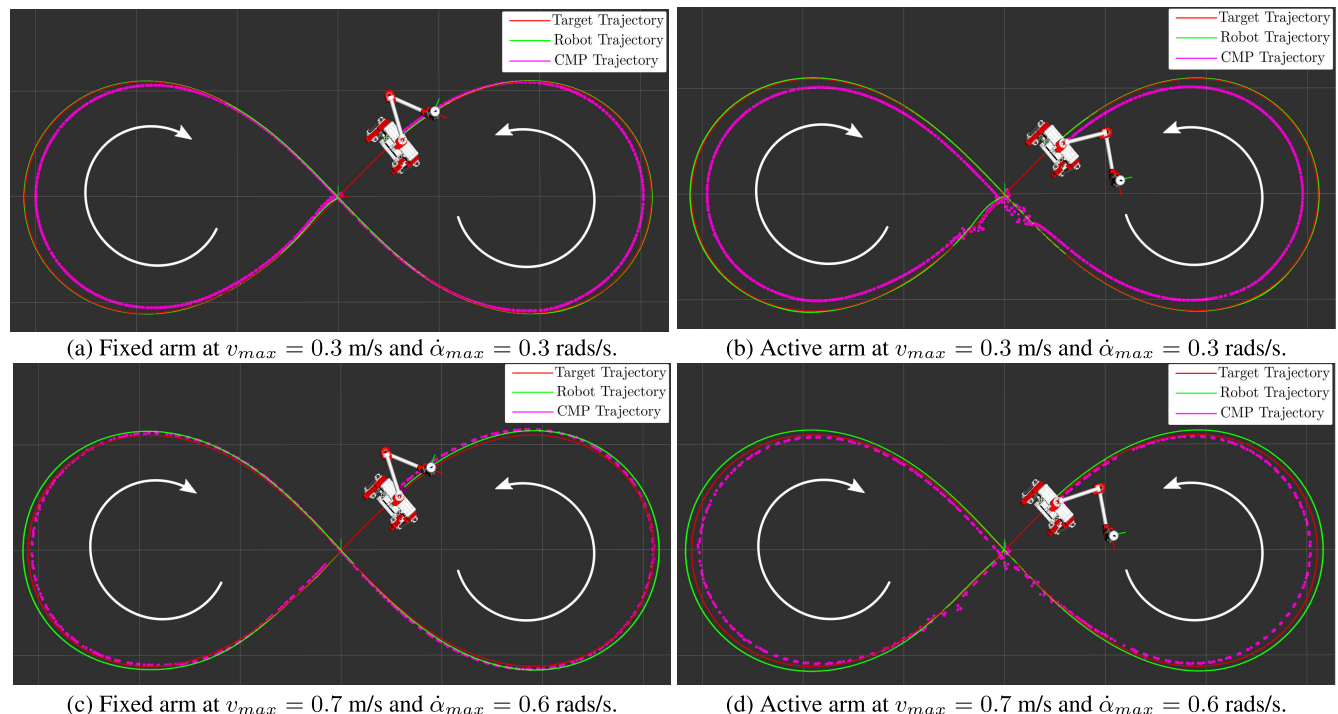


FIGURE 8. Infinity-loop trajectory tracking with the wheel-legged robot. By increasing motion speed, we observe the balance point indicated by CMP is going outward against the target trajectory for the fixed arm case. In contrast, by articulating the arm, this balance point can be manipulated toward the inside even at high speeds, which allows increasing balance stability margin even if there is outward centrifugal force during a curved trajectory tracking.

VI. DISCUSSION

The simulation results clearly demonstrate that the proposed arm acceleration control improves the overall translational and lateral stability of the wheel-legged self-balancing robot. However, this approach depends on the mass and inertia of the object carried by the end-effector and the initial configuration of the end-effector itself. The video

demonstration of the presented experiments is available at <https://youtu.be/KQ1mbQeLFtc>

Figure 7 shows the motion of the robot arm during a frontal push of 27 N. We can observe that the robot starts to accelerate its end-effector towards the forward position as soon as the force is applied, and once it returns to its reference position the end-effector also returns to the home configuration. The

first part of Table 2 shows how the arm acceleration with holding a typical can reduces the errors as the external force increases on the robot. However, it is also clear from the second part of the table that when the can mass is doubled the errors cannot be reduced after a certain level. This ascertains a fundamental limit on reducing the effects of external forces through the use of a manipulator arm. Indeed, this is a similar situation to the human movement. Humans use their arms to increase balance stability, but there is a certain limit related to the mechanical dynamics condition where the arm mass portion is limited against the total whole-body mass.

In addition, the use of the arm can increase the robot's maximum tolerance to the external linear push from 27 to 31.5 N with the typical can carrying task and 32.5 N when the mass of the can is doubled, an increase of 16.67% and 20.37% compared to the fixed arm case, respectively. This makes a significant contribution to the overall system stability. This concept would lead to the wheel-legged biped robot with an active arm for dual purposes, one is for carrying objects, another is for increasing the balance stability. This point is important for the future application of wheel-legged biped robots in a real-world environment with complex interactions.

VII. CONCLUSION AND FUTURE WORK

In this paper, we proposed and validated a novel scheme to improve the stability of a wheel-legged biped robot with active usage of its arm manipulator. To assess the system stability, we also used the CMP as an evaluation metric, which is commonly used for humanoid robots but had not been previously used for wheel-legged biped robots. Through several experiments, it was shown that the proposed method improved stability against translational disturbances and centrifugal and lateral forces when traversing curves at high speeds.

In future work we intend to apply and test the proposed method to a real robot. Furthermore, to improve the overall system stability, we plan to incorporate the roll motion of the robot by using its knee joints for uneven terrain.

REFERENCES

- [1] Boston Dynamics. *Introducing Handle*. Accessed: Feb. 28, 2017. [Online]. Available: <https://www.youtube.com/watch?v=-7xvqQeoA8c>
- [2] E. Koyanagi, S. Iida, K. Kimoto, and S. Yuta, "A wheeled inverse pendulum type self-contained mobile robot and its two-dimensional trajectory control," in *Proc. 2nd Int. Symp., Meas. Control Robot.*, 1992, pp. 891–898.
- [3] Y. Ha and S. Yuta, "Trajectory tracking control for navigation of self-contained mobile inverse pendulum," in *Proc. IEEE/RSJ Int. Conf. Intell. Robots Syst. (IROS)*, Sep. 1994, pp. 1875–1882.
- [4] N. Shiroma, O. Matsumoto, and K. Tani, "Cooperative behavior of a mechanically unstable mobile robot for object transportation," *JSME Int. J. Ser. C*, vol. 42, no. 4, pp. 965–973, 1999.
- [5] F. Grasser, A. D'Arrigo, S. Colombi, and A. C. Rufer, "JOE: A mobile, inverted pendulum," *IEEE Trans. Ind. Electron.*, vol. 49, no. 1, pp. 107–114, Feb. 2002.
- [6] M. Baloh and M. Parent, "Modeling and model verification of an intelligent self-balancing two-wheeled vehicle for an autonomous urban transportation system," in *Proc. Conf. Comput. Intell., Robot., Autonomous Syst.*, 2003, pp. 1–7.
- [7] K. Pathak, J. Franch, and S. K. Agrawal, "Velocity control of a wheeled inverted pendulum by partial feedback linearization," in *Proc. 43rd IEEE Conf. Decis. Control (CDC)*, Dec. 2004, pp. 3962–3967.
- [8] K. Pathak, J. Franch, and S. K. Agrawal, "Velocity and position control of a wheeled inverted pendulum by partial feedback linearization," *IEEE Trans. Robot.*, vol. 21, no. 3, pp. 505–513, Jun. 2005.
- [9] S. Jeong and T. Takahashi, "Wheeled inverted pendulum type assistant robot: Inverted mobile, standing, and sitting motions," in *Proc. IEEE/RSJ Int. Conf. Intell. Robots Syst.*, Oct. 2007, pp. 1932–1937.
- [10] S. Jeong and T. Takahashi, "Wheeled inverted pendulum type assistant robot: Design concept and mobile control," *Intell. Service Robot.*, vol. 1, no. 4, pp. 313–320, Oct. 2008.
- [11] M. Stilman, J. Olson, and W. Gloss, "Golem Krang: Dynamically stable humanoid robot for mobile manipulation," in *Proc. IEEE Int. Conf. Robot. Autom.*, May 2010, pp. 3304–3309.
- [12] J. Huang, Z.-H. Guan, T. Matsuno, T. Fukuda, and K. Sekiyama, "Sliding-mode velocity control of mobile-wheeled inverted-pendulum systems," *IEEE Trans. Robot.*, vol. 26, no. 4, pp. 750–758, Aug. 2010.
- [13] J.-X. Xu, Z.-Q. Guo, and T. H. Lee, "Design and implementation of integral sliding-mode control on an underactuated two-wheeled mobile robot," *IEEE Trans. Ind. Electron.*, vol. 61, no. 7, pp. 3671–3681, Jul. 2014.
- [14] F. Dai, X. Gao, S. Jiang, W. Guo, and Y. Liu, "A two-wheeled inverted pendulum robot with friction compensation," *Mechatronics*, vol. 30, pp. 116–125, Sep. 2015.
- [15] M. Zafar and H. I. Christensen, "Whole body control of a wheeled inverted pendulum humanoid," in *Proc. IEEE-RAS 16th Int. Conf. Humanoid Robots (Humanoids)*, Nov. 2016, pp. 89–94.
- [16] M. Zafar, S. Hutchinson, and E. A. Theodorou, "Hierarchical optimization for whole-body control of wheeled inverted pendulum humanoids," in *Proc. Int. Conf. Robot. Autom. (ICRA)*, May 2019, pp. 7535–7542.
- [17] Y. Xin, H. Chai, Y. Li, X. Rong, B. Li, and Y. Li, "Speed and acceleration control for a two wheel-leg robot based on distributed dynamic model and whole-body control," *IEEE Access*, vol. 7, pp. 180630–180639, 2019.
- [18] S. Xin, Y. You, C. Zhou, C. Fang, and N. Tsagarakis, "A torque-controlled humanoid robot riding on a two-wheeled mobile platform," in *Proc. IEEE/RSJ Int. Conf. Intell. Robots Syst. (IROS)*, Sep. 2017, pp. 1435–1442.
- [19] V. Klemm, A. Morra, C. Salzmann, F. Tschopp, K. Bodie, L. Gulich, N. Kung, D. Mannhart, C. Pfister, M. Vierneisel, F. Weber, R. Deuber, and R. Siegwart, "Ascento: A two-wheeled jumping robot," in *Proc. Int. Conf. Robot. Autom. (ICRA)*, May 2019, pp. 7515–7521.
- [20] V. Klemm, A. Morra, L. Gulich, D. Mannhart, D. Rohr, M. Kamel, Y. D. Viragh, and R. Siegwart, "LQR-assisted whole-body control of a wheeled bipedal robot with kinematic loops," *IEEE Robot. Autom. Lett.*, vol. 5, no. 2, pp. 3745–3752, Apr. 2020.
- [21] G. Zambella, G. Lentini, M. Garabini, G. Grioli, M. G. Catalano, A. Palleschi, L. Pallottino, A. Bicchi, A. Settimi, and D. Caporale, "Dynamic whole-body control of unstable wheeled humanoid robots," *IEEE Robot. Autom. Lett.*, vol. 4, no. 4, pp. 3489–3496, Oct. 2019.
- [22] S. Kim and S. Kwon, "Nonlinear optimal control design for underactuated two-wheeled inverted pendulum mobile platform," *IEEE/ASME Trans. Mechatronics*, vol. 22, no. 6, pp. 2803–2808, Dec. 2017.
- [23] L.-G. Lin and M. Xin, "Nonlinear control of two-wheeled robot based on novel analysis and design of SDRE scheme," *IEEE Trans. Control Syst. Technol.*, vol. 28, no. 3, pp. 1140–1148, May 2020.
- [24] K. J. Boström, T. Dirksen, K. Zentgraf, and H. Wagner, "The contribution of upper body movements to dynamic balance regulation during challenged locomotion," *Frontiers Hum. Neurosci.*, vol. 12, p. 8, Jan. 2018.
- [25] M. B. Popovic, A. Goswami, and H. Herr, "Ground reference points in legged locomotion: Definitions, biological trajectories and control implications," *Int. J. Robot. Res.*, vol. 24, no. 12, pp. 1013–1032, Dec. 2005.
- [26] M. Hayashibe, A. Gonzalez, and M. Tournier, "Personalized balance and fall risk visualization with Kinect two," in *Proc. 42nd Annu. Int. Conf. IEEE Eng. Med. Biol. Soc. (EMBC)*, Jul. 2020, pp. 4863–4866.
- [27] F. Raza, D. Owaki, and M. Hayashibe, "Modeling and control of a hybrid wheeled legged robot: Disturbance analysis," in *Proc. IEEE/ASME Int. Conf. Adv. Intell. Mechatronics (AIM)*, Jul. 2020, pp. 466–473.
- [28] F. Raza and M. Hayashibe, "Towards robust wheel-legged biped robot system: Combining feedforward and feedback control," in *Proc. IEEE/SICE Int. Symp. Syst. Integr. (SII)*, Jan. 2021, pp. 606–612.
- [29] B. Siciliano, L. Sciavicco, L. Villani, and G. Oriolo, *Robotics: Modelling, Planning and Control*. London, U.K.: Springer, 2009.
- [30] J. Luh, M. Walker, and R. Paul, "Resolved-acceleration control of mechanical manipulators," *IEEE Trans. Autom. Control*, vol. AC-25, no. 3, pp. 468–474, Jun. 1980.

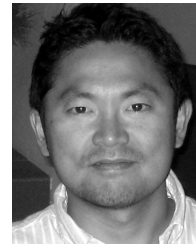
- [31] A. Goswami and V. Kallem, "Rate of change of angular momentum and balance maintenance of biped robots," in *Proc. IEEE Int. Conf. Robot. Autom. (ICRA)*, Apr./May 2004, pp. 3785–3790.
- [32] M. Popovic, A. Hofmann, and H. Herr, "Angular momentum regulation during human walking: Biomechanics and control," in *Proc. IEEE Int. Conf. Robot. Autom. (ICRA)*, Apr./May 2004, pp. 2405–2411.
- [33] D. Orin, "Interactive control of a six-legged vehicle with optimization of both stability and energy," Ph.D. dissertation, Dept. Elect. Eng., Ohio State Univ., Columbus, OH, Canada, 1976.
- [34] B.-S. Lin and S.-M. Song, "Dynamic modeling, stability and energy efficiency of a quadrupedal walking machine," in *Proc. IEEE Int. Conf. Robot. Autom.*, May 1993, pp. 367–373.
- [35] Open Source Robotics Foundation. *Gazebo*. Accessed: Jul. 2014. [Online]. Available: <http://gazebosim.org/>
- [36] Open Source Robotics Foundation. *ROS—Robot Operating System*. Accessed: Jul. 2014. [Online]. Available: <https://www.ros.org/>



FAHAD RAZA (Graduate Student Member, IEEE) received the B.S. degree in electrical engineering from Air University, Islamabad, Pakistan, in 2011, and the M.S. degree in electronics science and technology from the University of Michigan-Shanghai Jiao Tong University Joint institute, Shanghai, China, in 2017. He is currently pursuing the Ph.D. degree with the Department of Robotics, Tohoku University, Sendai, Japan. From 2017 to 2018, he was a Research Assistant with the Robotics and Artificial Intelligence Laboratory, The Chinese University of Hong Kong, Shenzhen, China. His research interests include application of linear and nonlinear control to improve the system stability and robustness of safety-critical mobile robots.



WEI ZHU (Student Member, IEEE) received the B.S. degree in intelligent science and technology and the M.S. degree in control science and engineering from Nankai University, Tianjin, China, in 2017 and 2020, respectively. He is currently pursuing the Ph.D. degree in robotics with Tohoku University, Sendai, Japan. His research interests include reinforcement learning, path planning and tracking, and control of wheeled bipedal robot.



MITSUHIRO HAYASHIBE (Senior Member, IEEE) received the B.S. degree from the Tokyo Institute of Technology, in 1999, and the M.S. and Ph.D. degrees from the Graduate School of Engineering, The University of Tokyo, in 2001 and 2005, respectively. From 2001 to 2006, he was an Assistant Professor with the Department of Medicine, Jikei University School of Medicine. In 2007, he was a Postdoctoral Fellow with the Institut National de Recherche en Informatique et en Automatique (INRIA) and the Laboratoire d'Informatique, de Robotique et de Microélectronique de Montpellier (LIRMM), CNRS/University of Montpellier, France. Since 2008, he has been a tenured Research Scientist with INRIA and the University of Montpellier. Since 2012, he has been a Visiting Researcher with the RIKEN Brain Science Institute and TOYOTA Collaboration Center. Since 2017, he has been a Professor with the Department of Robotics, Tohoku University, and founder of the Neuro-Robotics Laboratory. He is currently a Senior Member of the IEEE Engineering in Medicine and Biology Society. He was a recipient of the 15th Annual Delsys Prize 2017 for Innovation in Electromyography from De Luca Foundation, USA. He serves as the Technical Activity Board Member for the International Foundation of Robotics Research (IFRR).